ORIGINAL RESEARCH ARTICLE

Design of a Frequency Multiplier Based on Laterally Coupled Quantum Dots for Optoelectronic Device Applications in the Terahertz Domain: Impact of Inhomogeneous Indium Distribution, Strain, Pressure, Temperature, and Electric Field

M. Choubani[1] · N. Benzerroug[1]

Abstract

We have investigated the effects of size, hydrostatic pressure, temperature, electric field, and inhomogeneous indium distribution on sub-band electronic properties and the second harmonic generation (SHG) coefficient. In our model, a system of two lens-shaped $In_xGa_{1-x}As$ quantum dots (QDs) laterally coupled to their wetting layer (WL) was investigated. To compute energy levels and their corresponding envelope functions, the finite difference method was used. Then, the SHG coefficient was calculated using the density matrix approach. The results showed that the indium segregation inside the WL and In–Ga interdiffusion inside QDs must be considered to match photoluminescence (PL) data. It was also found that the structure under study can be used to generate a stronger SHG coefficient in the terahertz domain. In addition, the SHG spectra can be adjusted with the inclusion of the hydrostatic pressure (P), temperature (T), spacer width (L_H) between neighboring QDs, and electric field (F) effects. Therefore, a redshift (to lower energies) or blueshift (to higher energies) of the SHG spectra can occur in the terahertz region, and the structure can be used as a frequency doubler.

Graphical Abstract
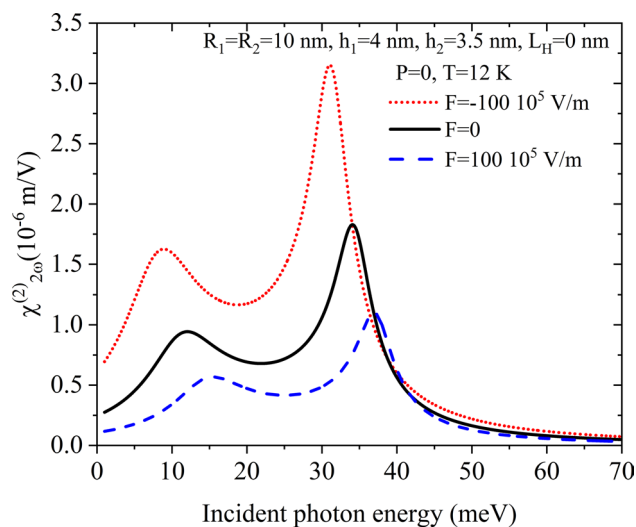
Keywords Atomic interdiffusion · electric field · indium segregation · hydrostatic pressure · second harmonic generation · temperature

Introduction

In recent years, the second (SHG) and third harmonic (THG) generations, nonlinear optical rectification (NOR), nonlinear absorption coefficient, and refractive index change coefficient have attracted increasing interest in technology applications. For example, Solaimani et al. examined the interdiffusion phenomenon and electric field effects on the NOR coefficient of GaAs/AlGaAs quantum wells (QWs).[1] Their results showed that the magnitude and peak position of NOR can be adjusted using parameters such as aluminum concentration and electric field intensity. In 2017, Mahdi et al.[2] studied the effect of temperature (T) on the band structure and confined energy states in pyramidal InGaAs/GaAs quantum dots (QDs). Souaf et al.[3] explored the indium segregation phenomenon in strained InGaAs/GaAs QWs and found that emission energy shifted to red (lower energy) with an increase in the segregation coefficient. The temperature and excitation power dependence of photoluminescence (PL) spectra of a bimodal size distribution of small and large InAs QDs was examined by Lee et al.[4] Their results showed that the major peak of the PL spectra was attributed to the ground state of the large QD, while the high-energy and minor peaks were attributed to the contributions of the ground and excited states of small and large QDs, respectively. The combined effects of the confinement potential and semispherical GaAs/AlGaAs QD radius were investigated by Mohammadi et al.,[5] which revealed that the NOR, SHG, and THG spectra shifted to red with an increase in the QD radius and to blue with an increase in the confinement potential height. Yahyaoui et al.[6] also showed that energy levels and carrier potential in self-assembled QDs coupled to their wetting layer (WL) were strongly affected by strain and interdiffusion phenomena. Therefore, any modeling of In(Ga)As QDs without indium segregation and interdiffusion phenomena will remain descriptive.[7–10] However, other reviews account for indium segregation or only lateral diffusion on surfaces during the epitaxial growth process of QDs.[11–13]

A large majority of these previous works are based on single QDs or QWs with or without indium segregation and In-Ga atomic intermixing. Also, the effects of temperature, electric field, pressure, strain, and QD morphology on the nonlinear optical properties (NLOP) are not considered simultaneously. Therefore, in the present paper, the effects of all the mentioned external factors on the SHG coefficient of laterally coupled lens-shaped InAs/GaAs QDs will be investigated in detail. Indium segregation inside the WL and atomic intermixing inside the QDs are modeled by Muraki's model and Gaussian distribution, respectively. The purpose is to correlate with the PL measurements and then adjust our results for terahertz applications using laterally coupled QDs. The remainder of this paper is organized as follows. The "Theoretical procedures" section explains the numerical method used to solve the three-dimensional (3D) Schrödinger equation, the inhomogeneous indium profiles used, and the SHG coefficient expressed in the density matrix approach. The results and discussion are then presented, and finally, our findings are summarized in the conclusion.

Theoretical Procedures

Due to a lattice mismatch of about 7% between the active layer (InAs) and the buffer material (GaAs), the strain effect switches the active layer towards three-dimensional (3D) islands called quantum dots (QDs) and leads to the formation of a two-dimensional (2D) layer known as a wetting layer (WL) with a thickness of about 2 MLs ≈ 5 Å.[14] Such a structure can be fabricated using the Stranski–Krastanov growth method[15] and molecular beam epitaxy (MBE).[16] Since the growth process leads to a bimodal distribution of QDs, the lateral coupling of QDs has been the subject of much research, and the investigation of the spacer width between QDs is of great importance in tailoring electronic and optical properties at the nanometer scale. In this work, our attention will be focused on the investigation of the SHG coefficient in two neighbored lens-shaped In$_x$Ga$_{1-x}$As QDs laterally coupled to their WL as shown in Fig. 1.

As shown, both QDs are embedded in cubical GaAs barrier material with dimensions L_x, L_y, $L_z = 60 \times 60 \times 60$
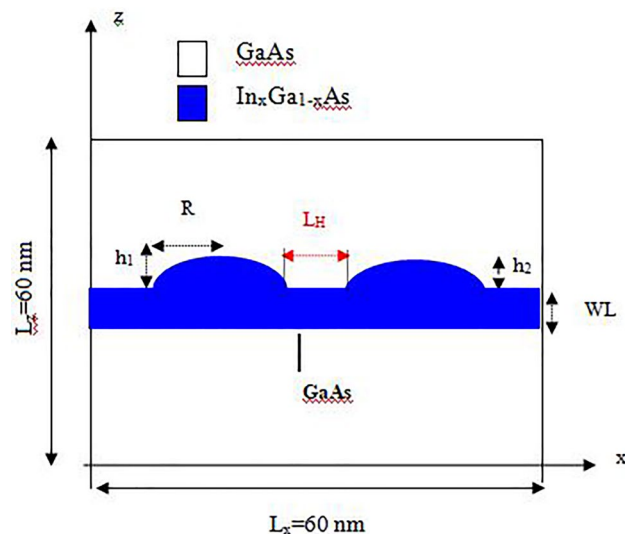

Fig. 1 A schematic cross section at $Y0 = 30$ nm of two neighbored lens-shaped InxGa1−xAs QDs laterally coupled to their WL with radius R and height h embedded in GaAs semiconductor material.

nm^3 along the x, y, and z directions, respectively. The left QD with radius R_1 and height h_1 is coupled to the right one with dimensions R_1 and h_2. In this work, the space width (L_H) between QDs will be used as an adjustment parameter to enhance the SHG coefficient in the terahertz domain. In this figure, X_0, Y_0, and Z_0 denote the cube center coordinates along the x, y, and z directions.

Also, during the epitaxy process of InAs well material on GaAs substrate, indium surface segregation occurs along the growth axis (z-axis) and inside the WL. This phenomenon is due to a difference in miscibility between the two semiconductors deposited. The impact of the indium segregation phenomenon was quantified by Muraki et al.[17] In this work, the impact of the indium segregation phenomenon was also introduced. Therefore, the indium composition in the nth monolayer is given by the following equations:

$$x(In) = \begin{cases} 0 \text{ in } GaAs \\ x_0\left(1 - R_x^n\right) \text{ for } 1 \leq n \leq N \\ x_0\left(1 - R_x^N\right)R_x^{n-N} \text{ for } n > N \end{cases} \tag{1}$$

where $R = 0.85$ is the segregation coefficient, $x_0 = 1$ denotes the nominal indium concentration, and N indicates the number of In$_x$Ga$_{1-x}$As monolayers grown before depositing the GaAs capping layer.

In addition, during the capping process with the GaAs material, the interchange of In and Ga atoms leads to diffusion in opposite directions from inside the QD to the GaAs barrier material and vice versa. This intermixing phenomenon leads to an inhomogeneous indium distribution inside the QD and consequently affects the energy band gap and the confined energy levels in the nanostructure. To introduce this random distribution of indium inside the QD, in this work we used a Gaussian function that takes into account the radial and vertical indium distribution inside the laterally coupled QDs. Therefore, the indium concentration is given by

$$x_{\text{In}}(r,z) = x_0 e^{-\left[\frac{(z-z_{L,R})^2}{2\sigma_z^2} + \frac{r^2}{2\sigma_r^2}\right]} \tag{2}$$

where

$$r = \sqrt{(x - X_0)^2 + (y - Y_0)^2}$$

$$\begin{cases} z_L = Z_0 - \dfrac{L_H}{2} + \alpha_z h_1 \text{ for the Left } QD \\ z_R = Z_0 + \dfrac{L_H}{2} + \alpha_z h_2 \text{ for the Right } QD \end{cases} \tag{3}$$

The standard deviations, σ_z and σ_r, along the growth axis and in the (xoy) section, respectively, are given by

$$\begin{cases} \sigma_{z,1,2} = \gamma_z h_{1,2} \\ \sigma_{r,1,2} = \beta_r r_{\text{QD1,2}}(z) \\ r_{\text{QD1,2}}(z) = R_{1,2}\sqrt{1 - \left(\dfrac{z - Z_{L,R}}{h_{1,2}}\right)^2} \end{cases} \tag{4}$$

where the index ($i = 1$, L) is used for the left QD and ($i = 2$, R) for the other neighboring QD placed on the right.

To compute the energy eigenvalues in the strained In$_x$Ga$_{1-x}$As/GaAs QDs, the 3D stationary Schrödinger equation given within the effective mass approximation is solved numerically[18]:

$$-\frac{h^2}{8\pi^2}\left[\overrightarrow{\nabla}\left(\frac{1}{m_{e,hh}^*(\vec{r},P,T)}\overrightarrow{\nabla}\right) + V(\vec{r},P,T) \pm q\vec{F}\vec{r}\right]\psi_i(\vec{r}) = E_i\psi_i(\vec{r}) \tag{5}$$

where $\vec{F}$ is the external applied electric field, $h = 6.62 \times 10^{-34}$, J·s is the Planck constant, V is the confining potential, and E_i and $\psi_i(\vec{r})$ are the energies and their corresponding wave functions, respectively.

The effective mass of the position-dependent electron is given by[19]

$$m_e^*(\vec{r},P,T) = \frac{m_0}{1 + 2\gamma + \left[\dfrac{E_P^\Gamma(E_g^\Gamma(P,T) + \frac{2}{3}\Delta_{S0})}{E_g^\Gamma(P,T)(E_g^\Gamma(P,T) + \Delta_{S0})}\right]} \tag{6}$$

where $m_0 = 9.1 \times 10^{-31}$ kg is the free electron mass. Δ_{S0}, E_p^Γ, and γ denote the spin–orbit splitting, the energy related to the momentum matrix element, and the Kane variable, respectively. The pressure (P) and temperature (T) unstrained band gap energy, E_g^Γ, is given by the following formula[20]:

$$E_g^\Gamma(P,T) = E_g^\Gamma(0,0) - \frac{\alpha T^2}{\beta + T} + \text{D.P} \tag{7}$$

The effective mass of the heavy hole as a function of the Luttinger parameters γ_1 and γ_2 is given by[19]

$$m_{hh}^*(\vec{r},P,T) = \frac{m_0}{\gamma_1 - 2\gamma_2} \tag{8}$$

The contribution of the hydrostatic strain (ε_h) and the biaxial strain ε_b to the band gap energy is given by[21,22]

$$\begin{cases} \varepsilon_h(r) = 2\left(\dfrac{a_0 - a_{\text{In}_x\text{Ga}_{1-x}\text{As}}(r)}{a_{\text{In}_x\text{Ga}_{1-x}\text{As}}(r)}\right)\left[1 - \dfrac{C_{12}(r)}{C_{11}(r)}\right] \\ \varepsilon_b(r) = 2\left(\dfrac{a_0 - a_{\text{In}_x\text{Ga}_{1-x}\text{As}}(r)}{a_{\text{In}_x\text{Ga}_{1-x}\text{As}}(r)}\right)\left[1 + \dfrac{2C_{12}(r)}{C_{11}(r)}\right] \end{cases} \tag{9}$$

where a_0 and $a_{\text{In}_x\text{Ga}_{1-x}\text{As}}$ are the lattice parameters of GaAs and In$_x$Ga$_{1-x}$As, respectively, and $C_{12}(r)$ and $C_{11}(r)$ are the position-dependent elastic stiffness constants of In$_x$Ga$_{1-x}$As.

Therefore, the strain-induced confinement potential for electrons in the conduction band is given by[23]

$$V_C(r) = \begin{cases} E_g(\text{GaAs}) - \Delta E_c(r) + a_c(r)\varepsilon_h(r), & \text{inside the WL and QDs} \\ E_g(\text{GaAs}), & \text{in GaAs barrier material} \end{cases}$$

(10)

where the band gap discontinuity for electrons is expressed as[20]

$$\Delta E_c(r) = 0.7\left[E_g(\text{GaAs}) - E_{g\text{In}_x\text{Ga}_{1-x}\text{As}}(r)\right]$$

(11)

and $a_c(r)$ is the position-dependent potential deformation.

In the valence band and for heavy holes, the confining potential as a function of the hydrostatic deformation potential, $a_v(r)$, and shear deformation potential, $b(r)$, is expressed as follows[19,23,24]:

$$V_B(r) = \begin{cases} \Delta E_v(r) + a_v(r)\varepsilon_h(r) + \frac{1}{2}b(r)\varepsilon_b(r), & \text{inside the WL and QDs} \\ 0, & \text{in GaAs material} \end{cases}$$

(12)

where the band gap discontinuity for heavy holes in the valence is given by[20]:

$$\Delta E_v(r) = 0.3\left[E_g(\text{GaAs}) - E_{g\text{In}_x\text{Ga}_{1-x}\text{As}}(r)\right]$$

(13)

Table I summarizes all the values of the physical quantities used in this calculation and for the two semiconductor materials InAs and GaAs. For all parameters of the strained $\text{In}_x\text{Ga}_{1-x}\text{As}$, we use Vegard's law as a function of the indium concentration and the bowing parameter (b_w)[25]:

Table I The material parameters of GaAs and InAs adopted from Refs. 17,19–25

Parameters	GaAs	InAs	b_w
$E_P^\Gamma(eV)$	28.8	21.5	0
Δ_{S0} (eV)	0.341	0.39	0.15
γ	−1.94	−2.9	0
γ_1	6.98	20.0	0
γ_2	2.06	8.5	0
Eg(0, 0) (eV)	1.519	0.533	0
α (meV/K)	0.5405	0.276	
β (K)	204	83	
a_{lattice} (Å)	5.6533	6.0584	0
a_c (eV)	−7.17	−5.08	2.61
a_v (eV)	1.16	1.0	0
b (eV)	−1.7	−1.8	0
C_{11} (10^{11} dyn cm^{-2})	11.879	8.329	0
C_{12} (10^{11} dyn cm^{-2})	5.376	4.526	0

$$P(\text{In}_x\text{Ga}_{1-x}\text{As}) = x_{\text{In}}(r)P(\text{InAs}) + (1 - x_{\text{In}}(r))P(\text{GaAs}) - b_w x_{\text{In}}(r)(1 - x_{\text{In}}(r))$$

(14)

where P can be the band gap energy, elastic stiffness constants, effective mass, etc.

By numerically solving the 3D Schrödinger equation, we can obtain the energy eigenvalues E_i and their corresponding envelope functions $\psi_i(\vec{r})$ in such a system. In this paper, we adopt the finite distance method (FDM).[26–28] This numerical method consists of uniform discretization of the computational domain (Fig. 1) with dimensions of $60 \times 60 \times 60$ nm^3 into $N_z = 241$ nodes along the X, Y, and Z directions, respectively. Thus, the discretization step is equal to $\Delta = 2.5$ Å. For simplicity, we denote each node (x_i, y_j, z_k) as (i, j, k) and the envelope function as $\psi_i(\vec{r}) = \psi_i(i, j, k)$, where i, j and $k = 1, 2, ... N_z$.

Generally, for better accuracy, we use the central difference approximation for the first-order derivative. For example, this derivative along the z-axis is given by

$$\frac{\partial \psi(i, j, k)}{\partial z} = \frac{\psi(i, j, k + 1) - \psi(i, j, k - 1)}{2\Delta}$$

(15)

Thus, we can convert the differential equation, Eq. (1), into a system of N_z^3 algebraic equations as follows:

$$A(i,j,k)\,\psi(i,j,k) + C(i+1,j,k)\,\psi(i+1,j,k) + E(i-1,j,k)\,\psi(i-1,j,k)$$
$$+B(i,j+1,k)\,\psi(i,j+1,k) + D(i,j-1,k)\,\psi(i,j-1,k)$$
$$+F(i,j,k+1)\,\psi(i,j,k+1) + G(i,j,k-1)\,\psi(i,j,k-1) = E\,\psi(i,j,k)$$

(16)

$$A(i,j,k) = \left(\frac{h}{4\pi\Delta}\right)^2 \left\{ \frac{6}{m*(i,j,k)} + \frac{1}{m*(i-1,j,k)} \right.$$
$$+ \frac{1}{m*(i+1,j,k)} + \frac{1}{m*(i,j-1,k)}$$
$$+ \frac{1}{m*(i,j+1,k)} + \frac{1}{m*(i,j,k-1)}$$
$$\left. + \frac{1}{m*(i,j,k+1)} \right\} + V(i,j,k)$$

$$C(i+1,j,k) = -\left(\frac{h}{4\pi\Delta}\right)^2 \left\{ \frac{1}{m*(i,j,k)} + \frac{1}{m*(i+1,j,k)} \right\}$$

$$E(i-1,j,k) = -\left(\frac{h}{4\pi\Delta}\right)^2 \left\{ \frac{1}{m*(i,j,k)} + \frac{1}{m*(i-1,j,k)} \right\}$$

$$B(i,j+1,k) = -\left(\frac{h}{4\pi\Delta}\right)^2 \left\{ \frac{1}{m*(i,j,k)} + \frac{1}{m*(i,j+1,k)} \right\}$$

$$D(i,j-1,k) = -\left(\frac{h}{4\pi\Delta}\right)^2 \left\{ \frac{1}{m*(i,j,k)} + \frac{1}{m*(i,j-1,k)} \right\}$$

$$F(i,j,k+1) = -\left(\frac{h}{4\pi\Delta}\right)^2 \left\{ \frac{1}{m*(i,j,k)} + \frac{1}{m*(i,j,k+1)} \right\}$$

$$G(i,j,k-1) = -\left(\frac{h}{4\pi\Delta}\right)^2 \left\{ \frac{1}{m*(i,j,k)} + \frac{1}{m*(i,j,k-1)} \right\}$$

(17)

Using the boundary conditions given by

$$\psi(i, j, k) \to 0 \text{ as } x, y, z \to \pm\infty$$

(18)

the problem comes down to solving $(Nz–2)^3$ linear equations, which are converted into a matrix H. Finally, the energy eigenvalues (E_i) and their corresponding envelope function ($\psi_i(\vec{r})$) can be obtained via diagonalization of H.

To confirm the reliability of our theoretical calculations, the optical transition energy of the conduction band to the heavy hole can be expressed as

$$E_{HH_1-E_i} = E_{HH_1} + E_i + E_g(In_xGa_{1-x}As) \tag{19}$$

where E_{HH1} is the hole energy of the ground state confined in the valence band, E_i is the electron energy of the ground ($i=1$) and first ($i=2$) excited states confined in the conduction band, and $E_g(In_xGa_{1-x}As)$ is the strained band gap energy.

Knowing E_i and Ψ_i, we are able to compute the second harmonic generation coefficient expressed in density matrix formalism[5,18,29]:

$$\chi_{2\omega}^{(2)} = \frac{N}{\varepsilon_0} \frac{\mu_{12}\mu_{23}\mu_{31}}{(E_{31} - 2h\omega + ih\Gamma_0)(E_{21} - h\omega + ih\Gamma_0)}, \tag{20}$$

where $N = 5 \times 10^{24}$ m^{-3} is the carrier density, GF $= \mu_{12}\mu_{23}\mu_{31}$ is the geometric factor, $\mu_{ij} = \langle \psi_i |ez| \psi_j \rangle$ denotes the dipole matrix element between the i and j states, $\omega_{res} = E_{ji} = (E_j - E_i)$ represents the energy of the transition between the i and j confined states, $\Gamma_0 = 1/T_0$, where $T_0 = 0.14$ ps is the relaxation time, and $\hbar\omega$ is the photon energy.

Results and Discussion

To obtain the best agreement between the calculated and measured data, we consider the same reference sample adopted by Maia et al.[30] In that work, the InAs QDs sample was grown on a 30-nm-thick GaAs substrate (001) using the MBE technique. During growth, the sample was kept at 510 °C, and a 2.2-monolayer InAs QD material was deposited on the GaAs substrate. The growth of such a system is finished by its encapsulation in 30 nm of the GaAs material. After GaAs capping, the cross-sectional scanning tunneling microscopy (XSTM) image obtained shows a typical lens-shaped InAs/GaAs with approximate height and base of $h=4$ nm and $2R=20$ nm, respectively. At a low temperature, $T=12$ K, the photoluminescence spectrum of this nanostructure adopted from Maia et al. shows the presence of two peaks, one centered at $E_{HH1-E1\_exp} = 1.068$ eV and the other at $E_{HH1-E2\_exp} = 1.141$ eV. The major peak located at E_{HH1-E1_exp} was attributed to the optical transition between the ground states E_1 and HH$_1$ confined in the conduction and valence bands, respectively. However, the minor peak located at E_{HH1-E2_exp} was assigned to the optical transition between

HH1 and the first excited state E_2 confined in the conduction band. Therefore, at a low temperature, the inter-sub-band transition energy is of the order of $E_{21} = E_2 - E_1 = 73$ meV.

In this paper, we proceed to investigate the correlation with experimental data. Therefore, we consider a strained single lens-shaped In$_x$Ga$_{1-x}$As QD with a base radius $R = 10$ nm and height $h = 4$ nm along the growth axis (001). Also, we consider that this QD is coupled with its WL subjected to strong segregation and intermixing effects that modify their size and composition considerably during the capping process.

Assuming homogeneous indium distribution ($x_{In} = 1$) we calculate the theoretical emission energies E_{HH1-E1_the} and E_{HH1-E2_the} at fixed QD height $h = 4$ nm as a function of the QD radius. As denoted in Fig. 2, it is clear that our computed results are far from the experimental data. However, when considering inhomogeneous indium distribution, the Gaussian distribution of indium in the QD was obtained with the adjustment parameters $\gamma_z = 0.5$, $\alpha_z = 0.62$, and $\beta_r = 0.8$. The indium distribution in the QD and the wetting layer after adjustment is depicted in Fig. 3b.

Accordingly, taking into account atomic intermixing and indium segregation, our results coincide with those obtained by measuring the PL of the considered structure based on QDs with a radius of 10 nm and height of 4 nm as illustrated in Fig. 2. The same figure shows a redshift of the optical emission energy with the increase in the QD radius, which can be explained by a reduction of the carrier confinement phenomenon.

The variation in the SHG coefficient versus the photon energy with and without the insertion of the indium segregation and atomic intermixing phenomena is presented
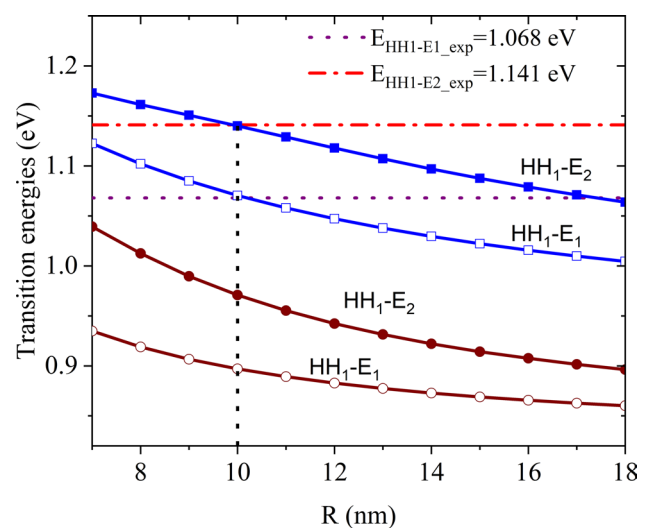
Fig. 2 The theoretical calculation of the optical transition energies versus the QD radius at low temperature $T = 12$ K, zero pressure, and a fixed QD height $h = 4$ nm.
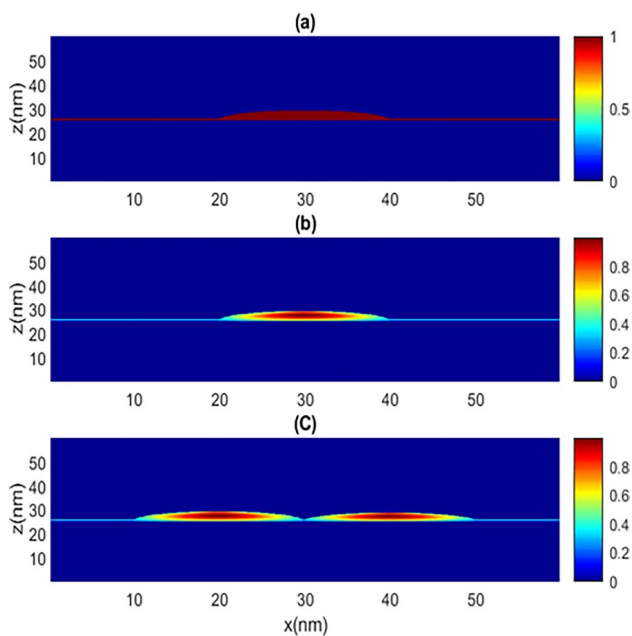
Fig. 3 A cross section of the 2D indium distribution inside the QD and inside the WL: (a) homogeneous, (b) and (c) inhomogeneous indium distributions.

in Fig. 4a. Here, it is clear that the SHG spectrum presents two peaks. The minor peak located at the transition energy $\omega_{r1} = E_2 - E_1 = E_{21}$ is attributed to the emission between the ground and the first excited levels confined in the conduction bands. Therefore, this peak is due to the absorption of one incident photon with energy $\hbar\omega$ as depicted in Fig. 4b. However, the major peak located at the resonant energy $\omega_{r2} = \frac{E_3 - E_1}{2} = \frac{E_{31}}{2}$ is attributed to the simultaneous absorption of two incident photons as depicted in Fig. 4c.

Accordingly, after the excitation of an electron from the ground state towards the first energy level confined in the conduction band, the electron relaxes with the emission of a signal having an energy ω_{r2}. Therefore, the structure can be used as a frequency doubler to generate the SHG from an input signal.

Furthermore, as shown in Fig. 4a, when the indium segregation inside the WL and In–Ga atomic interdiffusion in the QD are introduced, the transition energies ω_{r1} and ω_{r2} are blueshifted towards high energies and the SHG coefficient decreases in magnitude. Moreover, the computed inter-sub-band transition energy $\omega_{r1} = 73$ meV matches the PL experimental measurement. Therefore, to match experimental data, both the indium segregation and atomic intermixing phenomena must be taken into account in simulations.

As mentioned in the first section, to take into account the bimodal distribution of QDs, we have considered a system of two laterally coupled QDs having the same radius $R_1 = R_2 = 10$ nm. The left QD height is fixed at $h_1 = 4$ nm.

For this configuration, Fig. 3c shows the indium distribution inside the system of two strongly coupled QDs when the spacer width is fixed to zero, $L_H = 0$. The behavior of the lowest electron levels (E_1, E_2, and E_3: left axis) and the transition energies (ω_{r1} and ω_{r2}: right axis) as a function of the right QD height, h_2, at $T = 12$ K and zero pressure, $P = 0$, is depicted in Fig. 5. One can see a decrease in E_1, E_2, and E_3 when the right QD becomes wider than the left QD, which is a direct consequence of the reduction of the confinement phenomenon that shifts all the confined states down. We also observe that the energy difference between the ground state and the first excited state ($\omega_{r1} = E_2 - E_1$) increases with the increase in h_2 from 3 nm to 3 nm, and the same behavior is also seen for the transition energy $\omega_{r2} = \frac{E_3 - E_1}{2} = \frac{E_{31}}{2}$. Thus, for $h_2 < 4$ nm, it can be seen that the SHG spectrum displays a redshift towards low energies, and ω_{r1} and ω_{r2} remain in the terahertz domain. Hence, the confinement effect is dominated by the right QD with height $h_2 < h_1 = 4$ nm. Also, for this quenching QD height ($h_2 = 4$ nm), the two QDs are identical, and it should be pointed out that a level crossing occurs between the first confined states ($E_1 = E_2$).

This leads to two weakly coupled states well localized in each of the dots. Thus, for $h_2 = 4$ nm, the minor peak of the SHG spectrum has disappeared ($\omega_{r1} = E_2 - E_1$ tends to zero), and only the major peak persists. Therefore, only two energy levels are confined in such a system composed of two similar laterally coupled QDs. This behavior will be clarified in Fig. 7. However, for $h_2 > 4$ nm, a level splitting between the first excited states occurs, and the SHG spectrum experiences a blueshift towards high energies.

To understand the impact of the right QD height on the SHG intensity, we plot the resonant peak intensities $\chi^{(2)}_{2\omega\_\text{Max1}}$ and $\chi^{(2)}_{2\omega\_\text{Max2}}$ (left axis) and the geometric factor $\text{GF} = \mu_{12}\mu_{23}\mu_{31}$ (right axis) as a function of h_2, as depicted in Fig. 6. It can be seen that the SHG coefficient is directly proportional to the geometric factor, which decreases and tends to zero when the right QD height increases from $h_2 = 4$ nm to 13 nm.

To summarize the results of Figs. 5 and 6, for this system of two laterally coupled QDs, the SHG spectrum for three different values of h_2 is given in Fig. 7.

For $h_2 = 4$ nm, it can be seen that only the major peak appears with maximum intensity $\chi^{(2)}_{2\omega\_\text{Max}} = 4 \times 10^{-6}$ m/V. This is because the transition energy $\omega_{r1} = E_2 - E_1 = 0$ and the geometric factor $\text{GF} = \mu_{12}\mu_{23}\mu_{31}$ are highest, as depicted in Figs. 5 and 6, respectively. However, for $h_2 = 6$ nm and according to Fig. 5, the transition energy values of the two peaks of the SHG coefficient are $\omega_{r1} = 44.5$ meV and $\omega_{r2} = 43.3$ meV. Hence, the two peaks of the SHG spectrum are very close, and it seems only one peak is observed. Also, as compared to the $h_2 = 4$ nm case, the decrease in the SHG magnitude is attributed to a decrease in the geometric factor
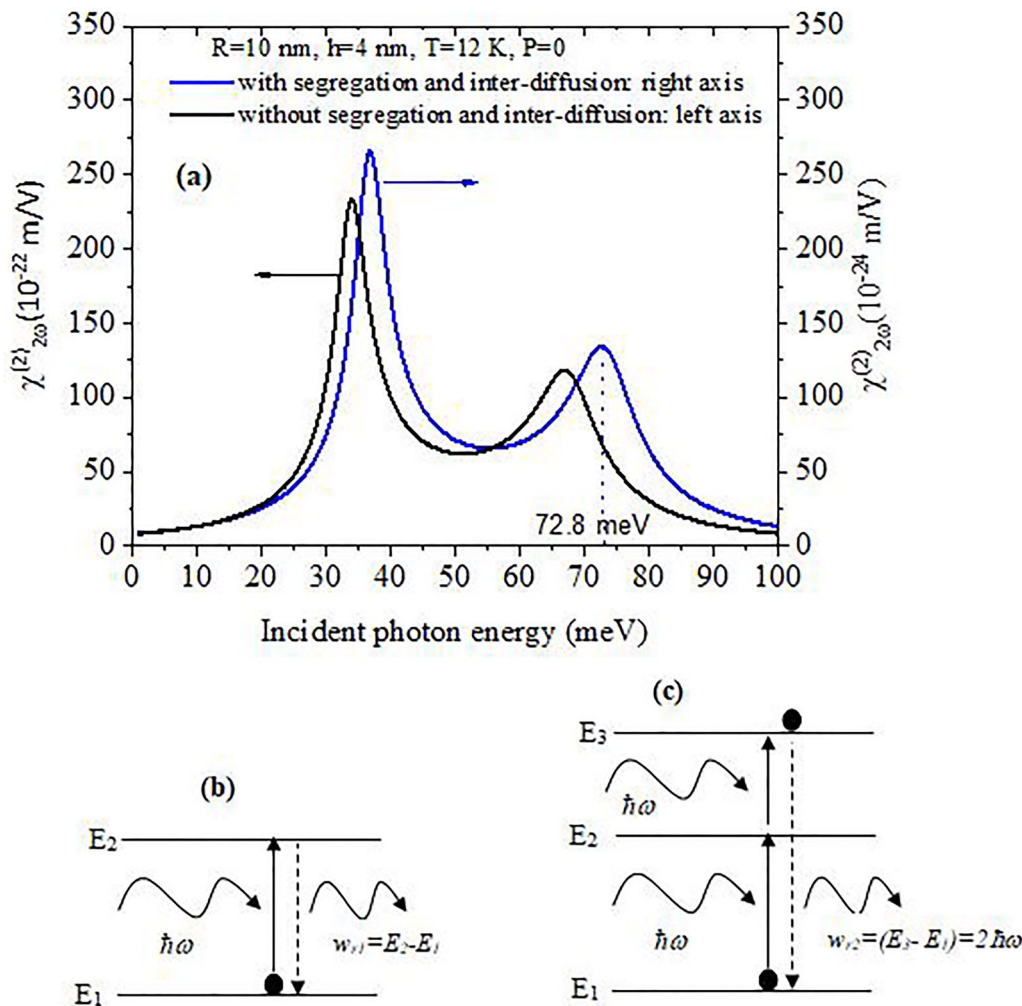
Fig. 4 (a) The second harmonic generation coefficient versus the photon energy under the impact of the indium segregation and In–Ga atomic interdiffusion phenomena for $R = 10$ nm, $h = 4$ nm, $T = 12$ K, and $P = 0$. (b) and (c) Schematic explanation of the minor and major peaks observed in the SHG spectrum, respectively.
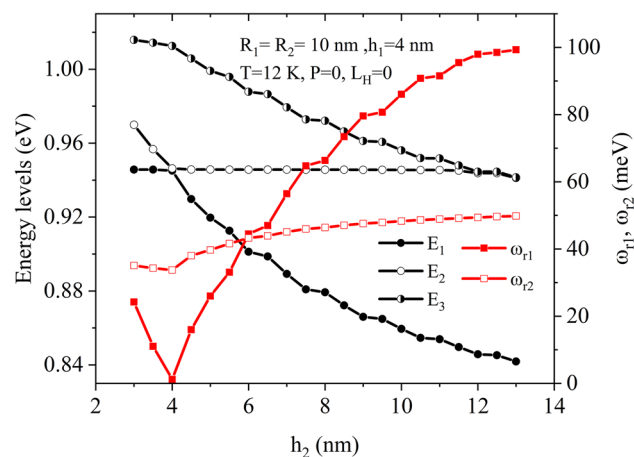
intensity from 6×10^{-27} to 1×10^{-27} m^3, as shown in Fig. 6. Therefore, the two SHG peaks are observed for a QD on the right side smaller than the one on the left. For this particular right QD height, $h_2 = 3.5$ nm $< h_1 = 4$ nm, the maximum value $\chi^{(2)}_{2\omega\_Max} = 1.8 \times 10^{-6}$ m/V of the SHG intensity is reached at the transition energy $\omega_{r2} = 34$ meV. Thus, to illustrate how to enhance the SHG intensity, the structural dimensions ($R_1 = 10$ nm, $h_1 = 4$ nm) and ($R_2 = 10$ nm, $h_2 = 3.5$ nm) will be investigated for all remaining computations.

Now, we explore the impact of the spacer on the peak intensity of the SHG as depicted in Fig. 8. The results reveal that the intensity decreases with an increase in the spacer width, L_H, between the right and left neighboring QDs. Hence, with an increase in the coupled width, the correlation between the QDs decreases and the system tends towards uncoupled and independent QDs for $L_H > 7$ nm. Thus,
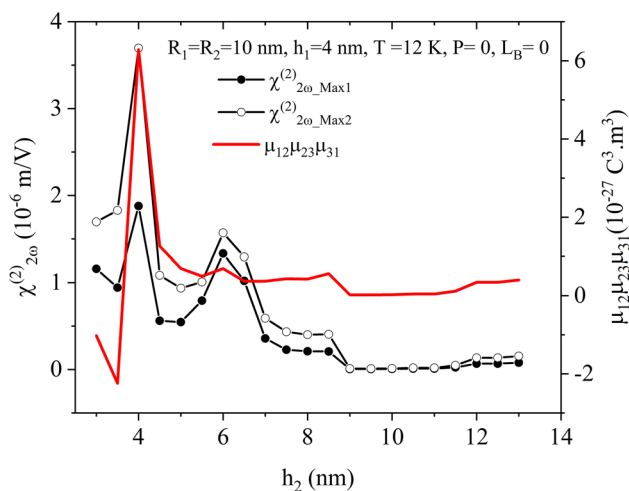

Fig. 5 Energy levels (left axis) and transition energies $\omega_{r1} = E_{21}$ and $\omega_{r2} = E_{31}/2$ (right axis) versus the right QD height for $R_1 = R_2 = 10$ nm, $h_1 = 4$ nm, $T = 12$ K, $P = 0$, and $L_H = 0$.

Fig. 6 Resonant peak values of the SHG coefficient (left axis) and the geometric factor $\mu_{12}\mu_{23}\mu_{31}$ (right axis) versus the right QD height for ($R_1 = 10$ nm, $h_1 = 4$ nm), $R_2 = 10$ nm, $T = 12$ K, $P = 0$, and $L_H = 0$.
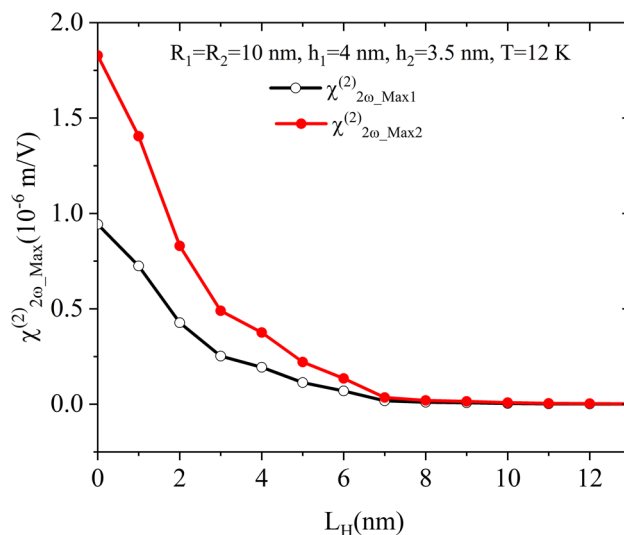

Fig. 8 The spacer effect (L_H) on the peak intensity of the SHG coefficient for ($R_1 = 10$ nm, $h_1 = 4$ nm), ($R_2 = 10$ nm, $h_2 = 3.5$ nm), $T = 12$ K, and $P = 0$.
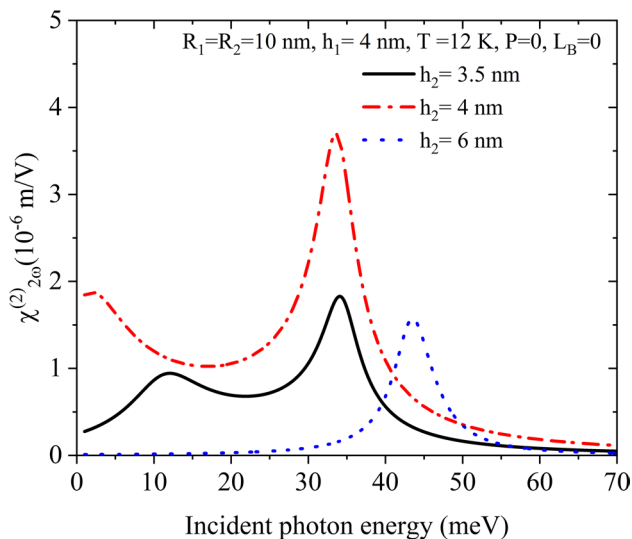

Fig. 7 Second harmonic generation versus the incident photon energy for three different values of the right QD height, where ($R_1 = 10$ nm, $h_1 = 4$ nm), $R_2 = 10$ nm, $T = 12$ K, $P = 0$, and $L_H = 0$.
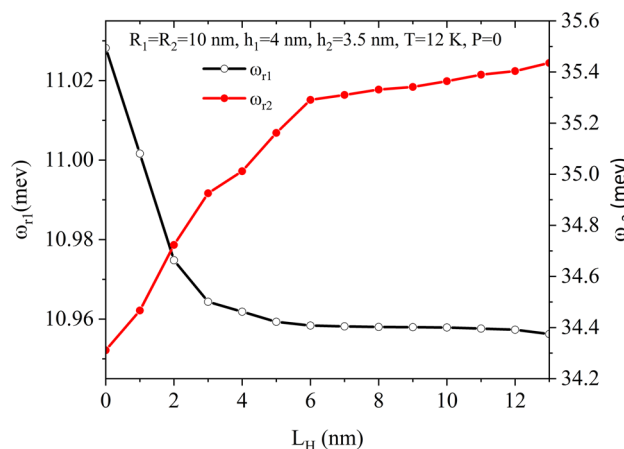

Fig. 9 Transition energies $\omega_{r1} = E_{21}$ and $\omega_{r2} = E_{31}/2$ versus the lateral coupled width L_H for ($R_1 = 10$ nm, $h_1 = 4$ nm), ($R_2 = 10$ nm, $h_2 = 3.5$ nm), $T = 12$ K, and $P = 0$.

when L_H is increased, the geometric factor GF = $\mu_{12}\mu_{23}\mu_{31}$ decreases, resulting in a decrease in the SHG intensity.

In addition, as depicted in Fig. 9, the minor peak position displays a redshift whereas the major peak experiences a blueshift in the terahertz domain. In other words, the optimal value of the SHG coefficient can be reached for a small spacer, $L_H = 0$, where QDs are strongly coupled to each other.

With the choice of $L_H = 0$, Fig. 10 shows the optimized SHG spectrum. As can be seen, the SHG intensity increases sevenfold as compared to uncoupled QDs when increasing the spacer width from $L_H = 0$ to 5 nm. Therefore, the space

width plays a significant role in optimizing the SHG spectrum for terahertz devices.

Also, Fig. 11 is plotted to investigate the impact of temperature (T) and hydrostatic pressure (P) on the SHG. It can be seen that the SHG magnitude decreases with increasing pressure from $P = 0$ kbar to 20 kbar. This behavior can be attributed to a decrease in the geometric factor GF = $\mu_{12}\mu_{23}\mu_{31}$ with increasing P. Additionally, the SHG spectrum experiences a blueshift to higher energies with increasing P. This phenomenon is associated with an increase in the confinement potential and carrier effective mass with increasing P. However, when the temperature is
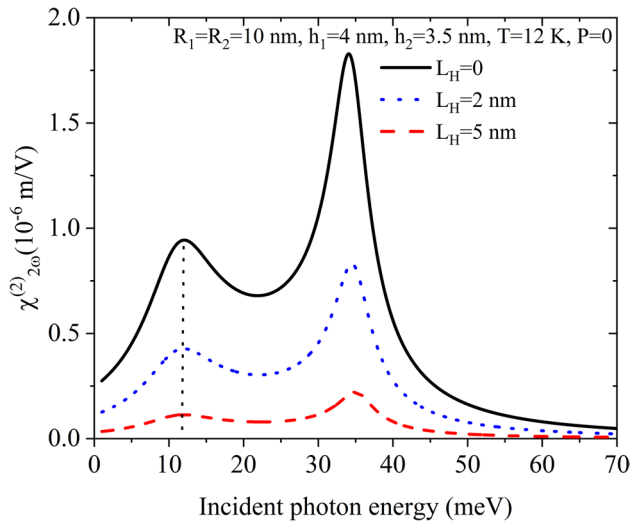
Fig. 10 Second harmonic generation versus the incident photon energy for three values of the lateral coupled width for ($R_1 = 10$ nm, $h_1 = 4$ nm), ($R_2 = 10$ nm, $h_2 = 3.5$ nm), $T = 12$ K, and $P = 0$.
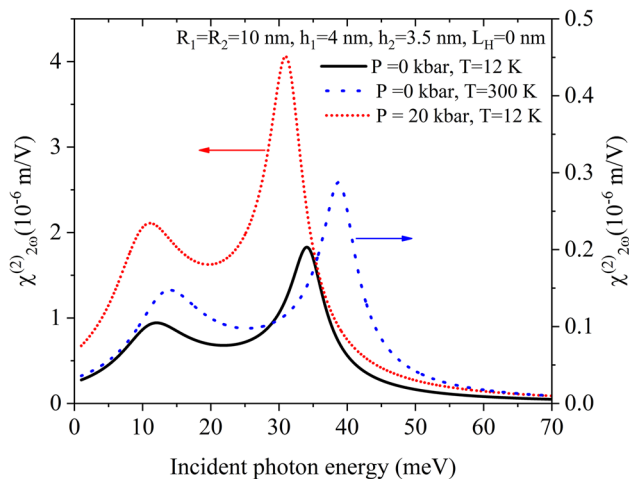

Fig. 11 Impact of temperature and hydrostatic pressure on the SHG spectrum for ($R_1 = 10$ nm, $h_1 = 4$ nm), ($R_2 = 10$ nm, $h_2 = 3.5$ nm), $T = 12$ K, $P = 0$, and $L_H = 0$.

increased from $T = 12$ K to 300 K, the reverse phenomenon is observed. Therefore, our results aid in understanding the pressure and temperature impacts on the SHG spectrum for terahertz applications.

To achieve greater consistency, we applied an external electric field to break the symmetry of the structure and increase the SHG intensity. As illustrated in Fig. 12, we see that the resonant peak values $\chi^{(2)}_{2\omega\_Max1}$ and $\chi^{(2)}_{2\omega\_Max2}$ are directly proportional to the geometric factor GF $= \mu_{12}\mu_{23}\mu_{31}$ and decrease along the entire range of applied electric field strength: $F = -100 \times 10^5$ to 100×10^5 V/m.
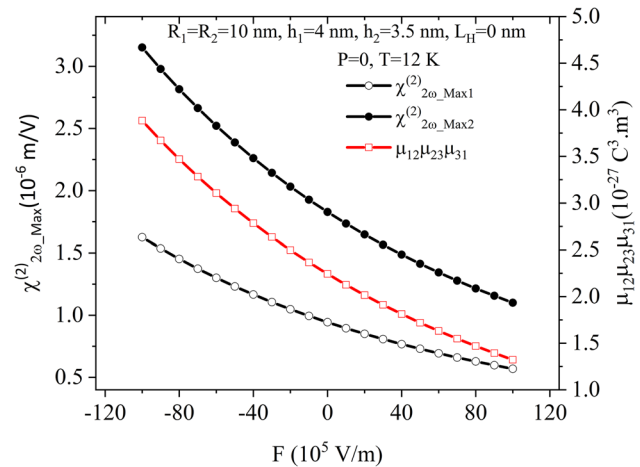

Fig. 12 Resonant peak values of the SHG coefficient and the geometric factor $\mu_{12}\,\mu_{23}\,\mu_{31}$ versus the electric field intensity for ($R_1 = 10$ nm, $h_1 = 4$ nm), ($R_2 = 10$ nm, $h_2 = 3.5$ nm), $T = 12$ K, $P = 0$, and $L_H = 0$.

In addition, it can be seen that a stronger SHG is obtained for an intense electric field, $F = -100 \times 10^5$ V/m, directed towards the substrate. In fact, the electric field breaks the symmetry of the structure. A negative field induces a downward tilt in the potential profile along the growth axis, while a positive field induces an upward tilt. Therefore, the amount of change in the overlapping between the electron envelope wave functions affects the dipole matrix elements, $\mu_{ij} = \langle \psi_i | ez | \psi_j \rangle$, between the confined states.

Consequently, the decrease in the minor and major peak intensities of the SHG coefficient can be explained by a decrease in the geometric factor when increasing the electric field magnitude.

Therefore, it is safe to say that the SHG magnitude is improved by applying an intense electric field, $F = -100 \times 10^5$ V/m, oriented towards the substrate. Also, the impact of the applied electric field requires more detailed study about how it also affects the resonant peak positions. Hence, the energies of the first three confined levels E_1, E_2, and E_3 versus the electric field intensity are plotted in Fig. 13.

The resonant energies ω_{r1} and ω_{r2} of the SHG peak positions are also depicted in Fig. 13, and show that energy levels suffer an apparent stark effect with an increase in F from -100×10^5 V/m to 100×10^5 V/m. Accordingly, both the minor peak and major peak of the SHG coefficient display a blueshift.

Figure 14 shows the SHG spectra of the optimized structure with and without the applied electric field.

As compared to the reference structure (for $F = 0$), the SHG intensity increases twofold and the spectrum displays a redshift under an applied electric field $F = -100 \times 10^5$ V/m oriented towards the substrate. Therefore, to generate a
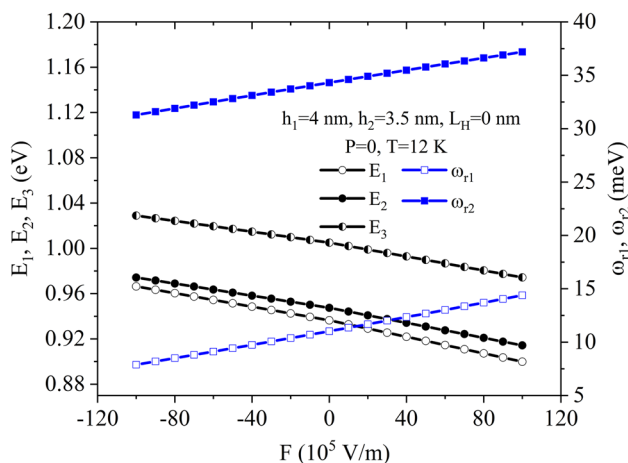
Fig. 13 The energies of the first three confined levels (E_1, E_2, and E_3) and transition energies $\omega_{r1} = E_{21}$ and $\omega_{r2} = E_{31}/2$ versus the electric field intensity for ($R_1 = 10$ nm, $h_1 = 4$ nm), ($R_2 = 10$ nm, $h_2 = 3.5$ nm), $T = 12$ K, $P = 0$, and $L_H = 0$.
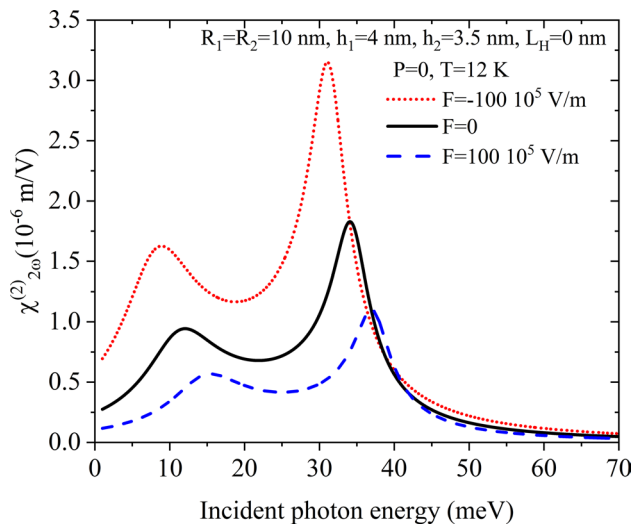

Fig. 14 SHG spectra of the optimized structure with and without the applied electric field for ($R_1 = 10$ nm, $h_1 = 4$ nm), ($R_2 = 10$ nm, $h_2 = 3.5$ nm), $T = 12$ K, $P = 0$, and $L_H = 0$.

stronger SHG coefficient, the results indicate that the structure under investigation can be used under intense and negative electric fields. However, under a positive electric field, the SHG spectrum displays a blueshift followed by a three-fold decrease in intensity. Thus, the results are encouraging and promising for the design of laterally coupled QDs based on the SHG coefficient in the terahertz domain with respect to the spacer width, indium segregation, and atomic intermixing phenomena.

Conclusion

In conclusion, the impacts of spacer width, electric field, strain, pressure, temperature, inhomogeneous indium distribution, and the morphology of single and laterally coupled lens-shaped QDs were investigated with respect to the energy eigenvalues, transition energies, dipole matrix elements, envelope functions, and SHG coefficient. Thus, the nanostructure was optimized to achieve a stronger SHG coefficient in the terahertz domain. The results reveal that inhomogeneous indium distribution due to segregation and intermixing phenomena must be considered in computations and must be controlled during the epitaxy process of such nanostructures to match the photoluminescence data. Accordingly, the inclusion of inhomogeneous indium distribution leads to a shift of the SHG spectrum to higher energies. In addition, as compared to a single QD, it was found that a system of two laterally coupled QDs can be used to generate a stronger SHG coefficient in the terahertz domain. Consequently, the SHG magnitude decreases with an increase in the spacer width between QDs, and the optimum SHG intensity is achieved for strongly coupled QDs. Moreover, our computed results reveal that the SHG spectrum displays a blueshift (redshift) with increasing temperature (pressure). Also, to generate a stronger SHG coefficient, the results reveal that the proposed structure can be used under intense and negative electric fields oriented towards the substrate and along the growth axis.

These results are encouraging and promising for the design of a frequency multiplier in the terahertz domain. In addition, this study offers the opportunity to explore other nonlinearities based on vertically coupled QDs considering inhomogeneous indium distribution phenomena in future work.

References

1. M. Solaimani, and H. Moghadam, Effects of interdiffusion and electric field on the optical rectification coefficient of GaAs/$Al_wGa_{1-w}As$ systems: crossover from single to multiple quantum wells. *Appl. Phys. A* 126, 278 (2020). https://doi.org/10.1007/s00339-020-3464-1.

2. M.A. Borgi, A. Reyahi, E. Jae, and M. Ghahremani, Effect of temperature on $In_xGa_{1-x}As$/GaAs quantum dots. *Pramana J. Phys.* 89(25), 1–7 (2017). https://doi.org/10.1007/s12043-017-1424-x.

3. M. Souaf, M. Baira, H. Maaref, and B. Ilahi, Modelling the intermixing effects in highly strained asymmetric InGaAs/GaAs quantum well. *Condens. Matter Phys.* 18(3), 33005 (2015). https://doi.org/10.5488/CMP.18.33005.

4. S.J. Lee, J.I. Lee, M.D. Kim, S.K. Noh, S.K. Kang, and J.W. Choe, Photoluminescence study of InAs quantum dots with a bimodal size distribution. *J. Korean Phys. Soc.* 42(5), 686–690 (2003).

5. S.A. Mohammadi, R. Khordad, and G. Rezaei, Optical properties of a semispherical quantum dot placed at the center of a cubic quantum box: optical rectification, second and third-harmonic generations. *Physica E* 76, 203–208 (2016). https://doi.org/10.1016/j.physe.2015.10.016.

6. M. Yahyaoui, K. Sellami, S. Ben Radhia, K. Boujdaria, M. Chamarro, B. Eble, C. Testelin, and A. Lemaître, Effects of strain on the optoelectronic properties of annealed InGaAs/GaAs self-assembled quantum dots. *Semicond. Sci. Technol.* 29(7), 075013 (2014).

7. Y. Arakawa, and M.J. Holmes, Progress in quantum-dot single photon sources for quantum information technologies: a broad spectrum review. *Appl. Phys. Rev.* 7, 021309 (2020). https://doi.org/10.1063/5.0010193.

8. Wu. Jiang, S. Chen, A. Seeds, and H. Liu, Quantum dot optoelectronic devices: lasers, photodetectors and solar cells. *J. Phys. D Appl. Phys.* 48, 363001 (2015). https://doi.org/10.1088/0022-3727/48/36/363001.

9. A.D. Yoffe, Semiconductor quantum dots and related systems: Electronic, optical, luminescence and related properties of low dimensional systems. *Adv. Phys.* 50, 1–208 (2001). https://doi.org/10.1080/00018730010006608.

10. P. Senellart, G. Solomon, and A. Andrew White, High-performance semiconductor quantum-dot single-photon sources. *Nat. Nanotechnol.* 12, 1026–1039 (2017). https://doi.org/10.1038/nnano.2017.218.

11. S. Kiravittaya, A. Rastelli, and O.G. Schmidt, Advanced quantum dot configurations. *Rep. Prog. Phys.* 72, 046502 (2009). https://doi.org/10.1088/0034-4885/72/4/046502.

12. A. Bruce, D. Joyce, and D. Vvedensky, Self-organized growth on GaAs surfaces. *Mater. Sci. Eng. R* 46, 127–176 (2004). https://doi.org/10.1016/j.mser.2004.10.001.

13. Fundamental physics and device applications, Skolnick M. S., Mowbray. D.J., Self-assembled semiconductor quantum dots. *Annu. Rev. Mater. Res.* 34, 181–218 (2004). https://doi.org/10.1146/annurev.matsci.34.082103.133534.

14. M. Cusack, P. Briddon, and M.A. Jaros, Electronic structure of InAs/GaAs self-assembled quantum dots. *Phys. Rev. B* 54, 2300 (1996). https://doi.org/10.1103/PhysRevB.54.R2300.

15. J.S. Samesta, B. Tongbram, D. Panda, D. Das, and S. Chakrabarti, A comprehensive analysis of strain profile in the heterogeneously coupled Stranski-Krastanov (SK) on Submonolayer (SML) quantum dot heterostructures. *J. Alloys Compd.* 847, 156483 (2020). https://doi.org/10.1016/j.jallcom.2020.156483.

16. L. Wang, L. Wang, Y. Jiadong, Z. Hao, Y. Luo, C. Sun, Y. Han, B. Xiong, J. Wang, and H. Li, Abnormal Stranski-Krastanov mode growth of green InGaN quantum dots: morphology, optical properties, and applications in light-emitting devices. *ACS Appl. Mater. Interfaces* (2019). https://doi.org/10.1021/acsami.8b16767.

17. K. Muraki, S. Fukatsu, Y. Shiraki, and R. Ito, Surface segregation of In atoms during molecular beam epitaxy and its influence on the energy levels in InGaAs/GaAs quantum wells. *Appl. Phys. Lett.* 61(5), 557–559 (1992). https://doi.org/10.1063/1.107835.

18. S. Shao, K.-X. Guo, Z.-H. Zhang, N. Li, and C. Peng, Studies on the second-harmonic generations in cubical quantum dots with applied electric field. *Phys. B* 406, 393–396 (2011). https://doi.org/10.1016/j.physb.2010.10.078.

19. I. Vurgaftman, J.R. Meyer, and L.R. Ram-Mohan, Band parameters for III–V compound semiconductors and their alloys. *J. Appl. Phys.* 89(11), 5818–5827 (2001). https://doi.org/10.1063/1.1368156.

20. Gh. Safarpour, M. Moradi, and M. Barati, Hydrostatic pressure and temperature effects on the electronic energy levels of a spherical quantum dot placed at the center of a nano-wire. *Superlattices Microstruct.* 52, 687–696 (2012). https://doi.org/10.1016/j.spmi.2012.06.019.

21. S.L. Chuang, *Physics of optoelectronic devices* (New York: Wiley, 1995).

22. Ph. Lelong, and G. Bastard, Binding energies of excitons and charged excitons in GaAs/Ga(In)As quantum dots. *Solid Stat. Comm.* 98, 819 (1996). https://doi.org/10.1016/0038-1098(96)00024-5.

23. A.D.B. Maia, E.C.F. da Silva, A.A. Quivy, V. Bindilatti, V.M. de Aquino, and I.F.L. Dias, Simulation of the electronic properties of In x Ga 1 x As quantum dots and their wetting layer under the influence of indium segregation. *J. Appl. Phys.* 114, 083708 (2013). https://doi.org/10.1063/1.4818610.

24. G.L. Bir, and E. Pikus, *Symmetry and strain-induced effects in semiconductors* (New York: Wiley, 1974).

25. P.A. Khomyakov, M. Luisier, and A. Schenk, Compositional bowing of band energies and their deformation potentials in strained InGaAs ternary alloys: a first-principles study. *Appl. Phys. Lett.* 107, 062104 (2015).

26. L. Gong, Y.-C. Shu, J.-J. Xu, Q.-S. Zhu, and Z.-G. Wang, Numerical analysis on quantum dots-in-a-well structures by finite difference method. *Superlattices Microstruct.* 60, 311–319 (2013). https://doi.org/10.1016/j.spmi.2013.05.012.

27. M. Choubani, H. Maaref, and F. Saidi, Tuning nonlinear optical properties in single lens-shaped core/shell under combined effects of temperature, pressure, transverse electric and magnetic fields. *J. Nanotech. Smart Mater.* 7, 101 (2021).

28. W.C. Yek, G. Gopir, and A.P. Othman, Calculation of electronic properties of InAs/GaAs cubic, spherical and pyramidal quantum dots with finite difference method. *Adv. Mater. Res.* 501, 347–351 (2012). https://doi.org/10.4028/www.scientific.net/AMR.501.347.

29. C. Chang, X. Li, Y. Duan, and Z. Zhao, Effects of hydrostatic pressure and temperature on the second-harmonic generation of spherical quantum dots with inversely quadratic Hellmann potential. *Indian J. Phys.* 97(5), 1–7 (2022). https://doi.org/10.1007/s12648-022-02507-9.

30. A.D.B. Maia, E.C.F. da Silva, A.A. Quivy, V. Bindilatti, V.M. de Aquino, and I.F.L. Dias, The influence of different indium-composition profiles on the electronic structure of lens-shaped In$_x$Ga$_{1-x}$As quantum dots. *J. Phys. D Appl. Phys.* 45, 225104 (2012). https://doi.org/10.1088/0022-3727/45/22/225104.

Authors and Affiliations

M. Choubani[1] · N. Benzerroug[1]

✉ M. Choubani
mohsenchoubani3@yahoo.fr

N. Benzerroug
benzerrougnabil@gmail.com

[1] Laboratory of Micro-Optoelectronics and Nanostructures (LR99ES29), Scientific Faculty, University of Monastir, 5019 Monastir, Tunisia